doi:10.20944/preprints201608.0224.v2

Peer-reviewed version available at *J. Mar. Sci. Eng.* **2016**, *4*, 70; doi:10.3390/jmse4040070

Article

Propeller Cavitation in Non-Uniform Flow and Correlation with the Near Pressure Field §

Francisco Alves Pereira *, Fabio Di Felice and Francesco Salvatore

CNR-INSEAN, Marine Technology Research Institute, Via di Vallerano 139, 00128 Rome, Italy; fabio.difelice@cnr.it (F.D.F.); francesco.salvatore@cnr.it (F.S.)

* Correspondence: francisco.alvespereira@cnr.it; Tel.: +39-06-502-99281

§ This paper is an extended version of our paper published in Proc. 25th Symposium on Naval Hydrodynamics, 2004, Vol. 4, 1-13.

Abstract: An experimental study is carried out in a cavitation tunnel on a propeller operating downstream of a non-uniform wake. The goal of this work is to establish quantitative correlations between the near pressure field and the cavitation pattern that takes place on the propeller blades. The pressure field is measured at the walls of the test section and in the near wake of the propeller, and is combined with quantitative high-speed image recording of the cavitation pattern. Through simple harmonic analysis of the pressure data and image processing techniques that allow to retrieve the cavitation extension and volume, we discuss the potential sources that generate the pressure fluctuations. Time correlations are unambiguously established between pressure peak fluctuations and cavitation collapse events, based upon the Rayleigh collapse time. Finally, we design a model to predict the cavitation-induced pressure fluctuations from the derivation of the cavitation volume acceleration. This simple model demonstrates a remarkable agreement with the actual pressure field.

Keywords: propeller; cavitation pattern; unsteady cavitation; induced pressure fluctuations; high-speed visualization; volume acceleration; cavitation-pressure correlations

---

1. Introduction

Cavitation occurrence on marine propellers or in hydraulic machinery is the source of undesirable effects: radiated noise, structural vibrations, erosion and loss of efficiency. In order to minimize these effects, the effort is put into the development of analysis tools capable of predicting, from the design stage and in an iterative optimization process, the propeller performance under cavitating conditions. The definition of these tools is dependent upon the experimental validation of current theoretical and numerical cavitating flow models [1].

The periodical motion through velocity discontinuities causes a periodic variation of the blade loading and of the hydrostatic pressure, thus modulating the thrust and torque developed by the propeller. This situation creates the necessary set of conditions favoring the inception of cavitation, and promotes the occurrence of fluctuating cavitation on the propeller blades, further enhanced by blade-to-blade geometrical differences. In the case of marine propellers, unsteady cavitation generates strong pressure fluctuations radiating through the water medium in the near field or to the submerged part of the hull structure, which then translates into structural vibrations and onboard noise. The broadband frequency content of the pressure field generated by cavitation makes it the major source of noise and vibrations on a ship, as it contributes to crew discomfort on a passenger vessel, interferes with scientific instrumentation on a research ship or compromises the stealth capabilities of a surface or underwater warship.

A relatively limited literature is available on the subject. Ito [2] investigated the effect of the flow angle of attack on the unsteady cavitation, using an oscillating blade and extrapolating the results to the propeller behind a hull. Increase in pressure fluctuations due to propeller cavitation was probably first reported by Takahashi and Ueda [3]. Huse [4] suggested that the cavity volume acceleration is the source mechanism of the hull pressure fluctuations induced by cavitation. Dyne [5] performed a general study on the scale effects on wake, propeller cavitation and induced pressure, but no direct correlations are established. Bark and Berlekom [6] have looked into the relations between cavity dynamics, type of cavitation and cavitation noise. The study was performed in a cavitation tunnel with an oscillating hydrofoil. In this work, the periodic growth of the cavity at the leading edge was found to increase the noise levels in the low frequency range, in particular at multiples of the oscillating blade frequency, whereas tip vortex cavitation and bubble cavitation generate high frequency noise. Matusiak [7] proposed a method to evaluate the noise contributions of the individual types of cavitation, respectively low-frequency pressure fluctuations from fixed blade cavitation and high-frequency broadband noise due to collapse of vapor bubbles. Several works report attempts to correlate the pressure and cavitation results obtained in a cavitation tunnel to those at fullscale [8,9]. Breslin *et al.* [10] presented an important theoretical and experimental research work directed at the prediction of pressure, forces and moments induced by intermittently cavitating propellers. Scale effects have been addressed for instance by Kurobe *et al.* [11] and Friesch *et al.* [12], who also considered pressure fluctuations at orders higher than twice or thrice the blade frequency [13]. More recently and with the help of high-speed video imaging, Johannsen [14] tried to derive distinct scaling laws based on fluid mechanical connections between cavity dynamics, time series of hull pressure and inflow velocity field. The bursting phenomenon of tip vortex cavitation has been investigated by Konno *et al.* [15] and recognized as a source of large pressure fluctuations. Paik *et al.* [16] performed a detailed velocimetry analysis of the propeller wake downstream of a hull, and used the proper order decomposition technique to identify the coherent flow structures. However, the effect on cavitation is not discussed. On the numerical side, Berger *et al.* [17] developed a simulation procedure to account for wake scale effects on hull pressure fluctuations. Volume acceleration and pressure amplitudes are compared at different scales but no direct relation is established. Also, Ji *et al.* [18] and later Ji *et al.* [19] performed numerical simulations of propellers operating in a non-uniform wake, concluding that "the acceleration due to the cavity volume changes is the main source of the pressure fluctuations excited by the propeller cavitation". However and to our best knowledge, no experimental verification of this claim has been clearly established nor quantified to this date.

The goal of this study is to gather the necessary information to verify in a quantitative manner the correlations between cavity volume acceleration and radiated pressure fluctuations. The current experiments are performed in a cavitation tunnel for a relevant range of cavitating flow conditions. Detailed temporal and spatial correlations are established between quantitative measurements of the cavitation pattern, and the pressure data measured at different locations in the vicinity of the propeller. The propeller used in this study, known as the INSEAN E779A propeller, has been extensively used and documented [e.g., 20]. The effect of the hull on the wake is simulated with an array of plates, which generates a localized non-uniformity in the propeller inflow, thus creating a periodical flow unsteadiness. The cavitation pattern measurements are established on the basis of automated image analysis of high-speed visualizations analyzed using correlation-based algorithms [1]. The pressure measurements are performed simultaneously at high frequency to provide an accurate time history for comparison with the time-resolved cavitation pattern data. Harmonic analysis is performed to investigate the energy content and establish spatial and temporal correlations with the pattern information. A model is finally implemented to describe the correlations with the cavitation pattern data, and compared with the actual data.

2. Experimental Setup

2.1. Facility and Propeller

The experiments are carried out at the Italian Navy cavitation tunnel facility (C.E.I.M.M.). The tunnel is a closed water circuit with a $0.6\,\mathrm{m}\times0.6\,\mathrm{m}\times2.6\,\mathrm{m}$ square test section. The propeller used in the present tests is a skewed four-blade model propeller, with a radius $R = D/2 = 0.1135\,\mathrm{m}$, a pitch-to-diameter ratio of 1.1 and a forward rake angle of 4.3°. The blockage ratio in the test section is about 10%.

The measurement configuration is pictured in Fig. 1. The propeller shaft is equipped with a rotary encoder that supplies one trigger pulse per rotation. This signal is used to pilot a pulse delay generator, which in turn drives the image and signal acquisition for phase-locked measurements. This rotation pulse is also recorded to time-mark the pressure signals, in particular for the purpose of ensemble statistics and harmonic analysis. This time marker also determines the start time of the image high-speed sequence and defines the 0° of the propeller angular position θ.

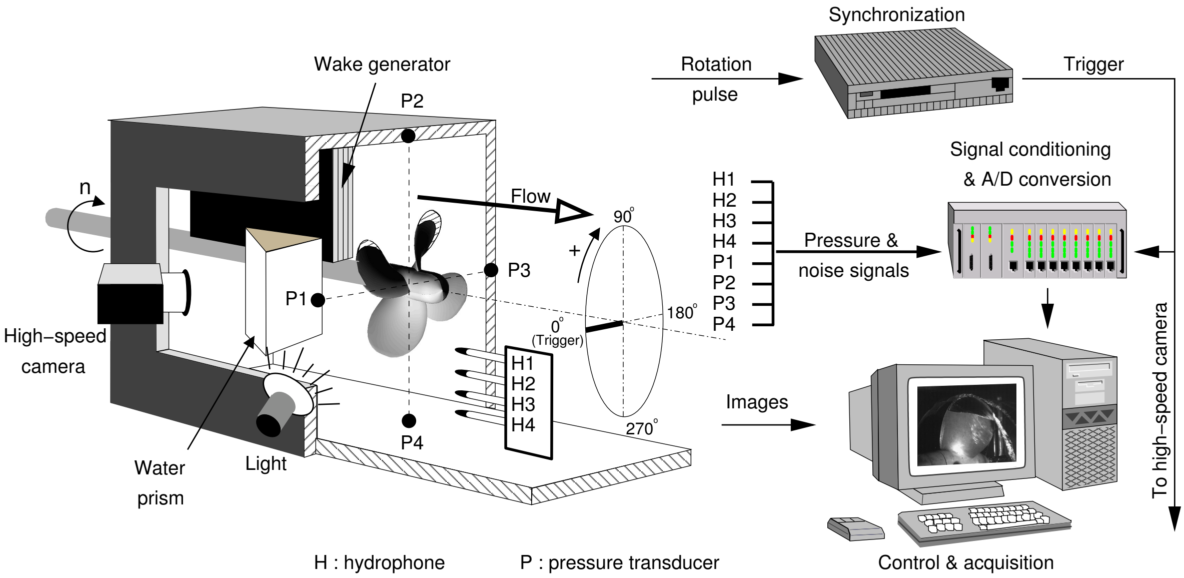

Figure 1. Experimental setup.

In the following sections, $J = U_\infty/nD$ and $K_T = T/\rho n^2 D^4$ are the advance and the thrust coefficients, respectively, with U_∞ being the upstream axial inflow velocity, n the propeller rotation velocity, ρ the fluid density and T the propeller thrust. The cavitation number $\sigma_0 = (p_0 - p_v)/\frac{1}{2}\rho U_\infty^2$ is related to the reference pressure p_0 measured at the propeller axis, and p_v is the vapor pressure.

2.2. Wake Generator

The non-uniformity of the wake downstream of a hull is here simulated using an array of plates, following closely the design described in the recommendation notes of the International Towing Tank Conference on measurements of hull pressure fluctuations [21]. The wake simulator, detailed in Fig. 2, is composed of five plates spaced 20 mm apart from each other and assembled together to form an array 86 mm wide, 232 mm high and 300 mm long. The rake is fixed to the roof of the test section, upstream of the propeller, as shown in the photograph.

The wake has been measured based on laser Doppler velocimetry. Figure 3 reports the velocity field in a crossflow plane, both in terms of mean and fluctuating quantities. Note that the mechanical structure of the wake generator has a visible signature on the velocity distributions.

2.3. Flow Conditions

The experiments are performed for a propeller rotation frequency n=30 Hz. The advance coefficient is adjusted to meet the thrust similitude between the K_T of the isolated propeller value, taken from previous performance tests in open water conditions, and that measured behind the wake simulator. The thrust coefficient K_T is set to 0.175, which leads to $J \approx 0.89$ for an upstream flow velocity of 6.22 m s^{-1}. The values of the cavitation number considered here vary from 8.0 to 2.5, with a step of 0.5. Note that the case $\sigma_0 = 8.0$ is considered a non-cavitating condition,

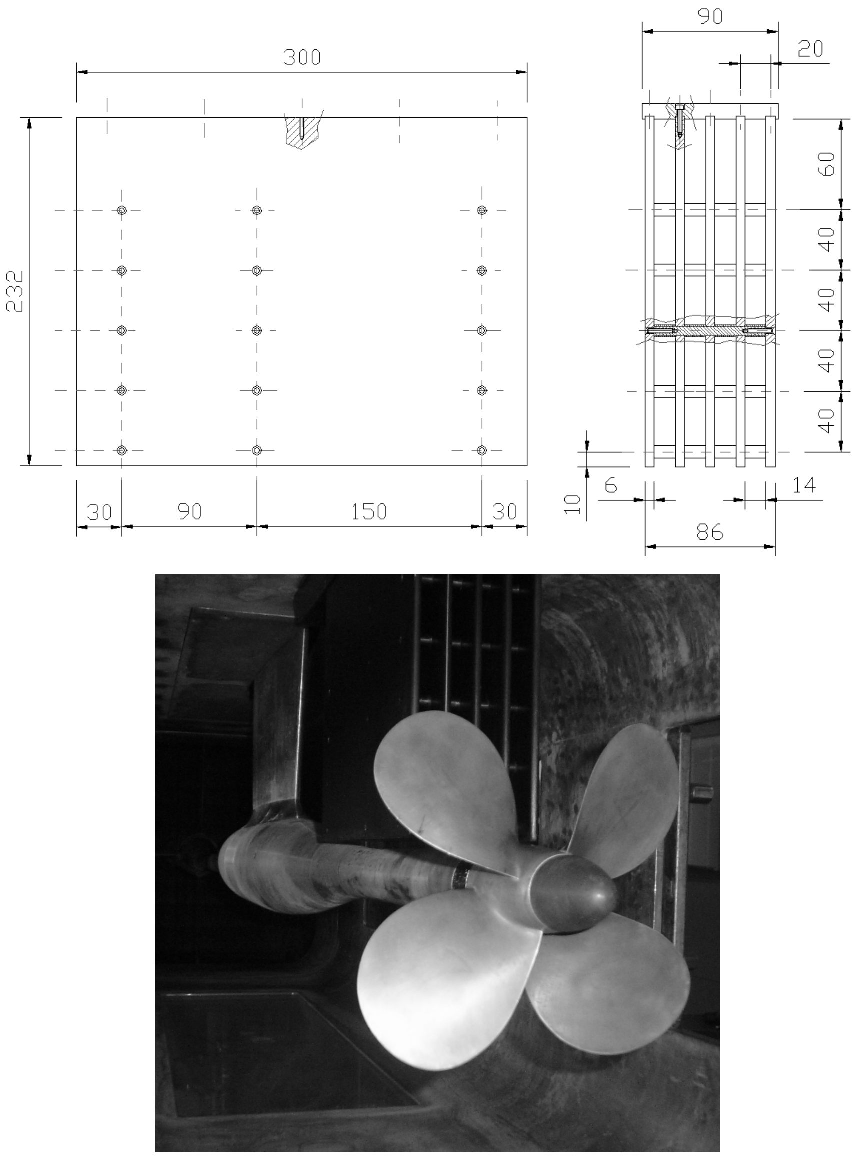

Figure 2. Non-uniform wake generator: design (top) and implementation in the cavitation tunnel (bottom). The dynamometer is mounted upstream.

although incipient cavitation would occur depending on the level of non-dissolved gas in the water and ambient temperature. The cavity extension is recorded for σ_0 equal to 7.5, 6.5, 5.5, 4.5, 3.5 and 2.5. A long period of water degassing is operated before starting the tests. The oxygen content is continuously monitored and is maintained below 5 ppm.

3. High-Speed Visualizations

A high-speed camera is used to record the cavitation pattern at a frame rate of 2000 frames per second with a resolution of 1024×1024 pixels. The rotation speed used in our experiments is 30 Hz, corresponding to an angular resolution of 5.4°. The camera is oriented at an angle with respect to the test section window, as depicted in Fig. 1. Since this arrangement would introduce strong optical aberrations, a glass tank in the form of a wedge and filled with water is placed against the window, such that the camera optical axis is normal to the wedge face. This solution minimizes the optical shortcomings of the non-normal viewing path. The illumination consists in a set of high-power flood lights to accommodate the short exposure time used to record the cavitation on the rotating blades,

doi:10.20944/preprints201608.0224.v2

Peer-reviewed version available at J. Mar. Sci. Eng. 2016, 4, 70; doi:10.3390/jmse4040070

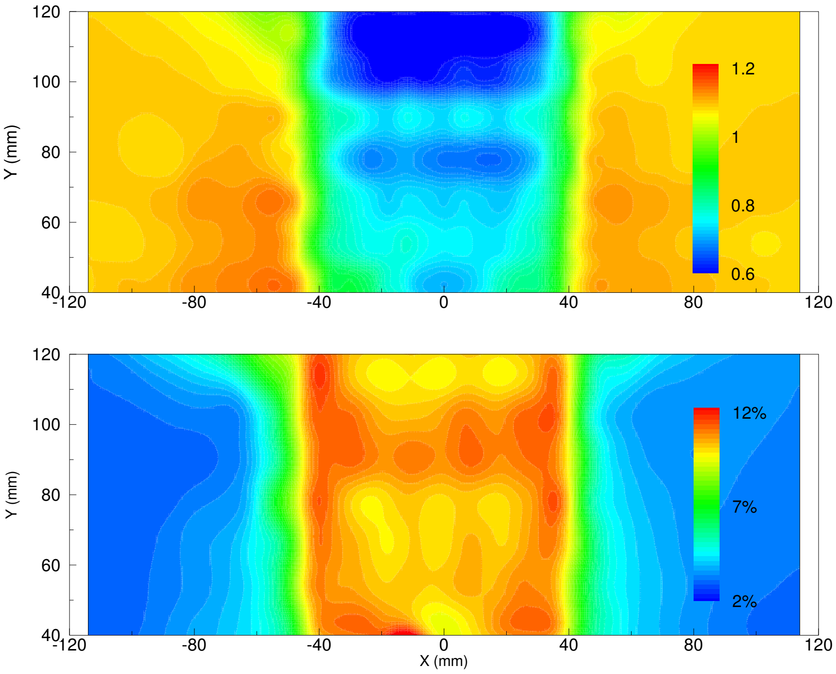

Figure 3. Non-uniform wake: mean velocity field normalized by the upstream flow velocity (top); velocity fluctuations in percentage of upstream flow velocity (bottom). Propeller axis is at (0, 0).

thus avoiding image blurring due to motion. A typical shutter time of 1/10000th to 1/20000th of a second is used. The method described by Pereira *et al.* [1], based on the cross-correlation of images with and without cavitation and on their non-linear geometrical transformation, is used to provide an accurate estimate of the mean and fluctuating cavity extension over the blades.

Figure 4 illustrates the cavitation pattern for a value of the cavitation number equal to 3.5, as the blade passes through the turbulent wake generated by the hull simulator. Such sequences are used to help interpret the pressure signals discussed later. They are further used to carry out quantitative information about the cavity pattern, specifically its mean extension and fluctuations.

The measurement of the cavity extension is performed on every frame. Each recording sequence lasts about 3 seconds, which is the maximum recording capacity of the system. During this time frame, the propeller performs approximately 90 revolutions. The camera is only triggered once to initiate the recording, simultaneously to the pressure data acquisition, and then works at a preset frequency (2000 frames per second) for the remaining acquisition time. The mean and fluctuating values of the cavity extension are calculated within angular slots centered at discrete angles. In our case, the slot angular step is set to 5.0°, which is close to the angular resolution of the imaging, and the statistics are estimated inside angular slots of ±2.5°, that is no overlapping is operated between slots. Note that the optical access limits the observation to angular positions ranging from 60° to 120°.

4. Pressure Measurements

4.1. Instrumentation

The pressure measurements are performed with four Endevco® model 8510C-15 piezo-resistive pressure transducers, flush mounted to the test section walls and placed on the propeller plane, as indicated on Fig. 1. These pressure transducers are designed by P_1, P_2, P_3 and P_4, and are placed at 0°, 90°, 180° and 270°, respectively. Note that P_2 is at 12-o'clock, above and closest to the propeller.

Four Brüel&Kjaer® 8103-type hydrophones fixed to a streamlined strut are used for the pressure measurements in the fluid, and are referred to as H_1, H_2, H_3 and H_4, see Fig. 1. The sensors are located

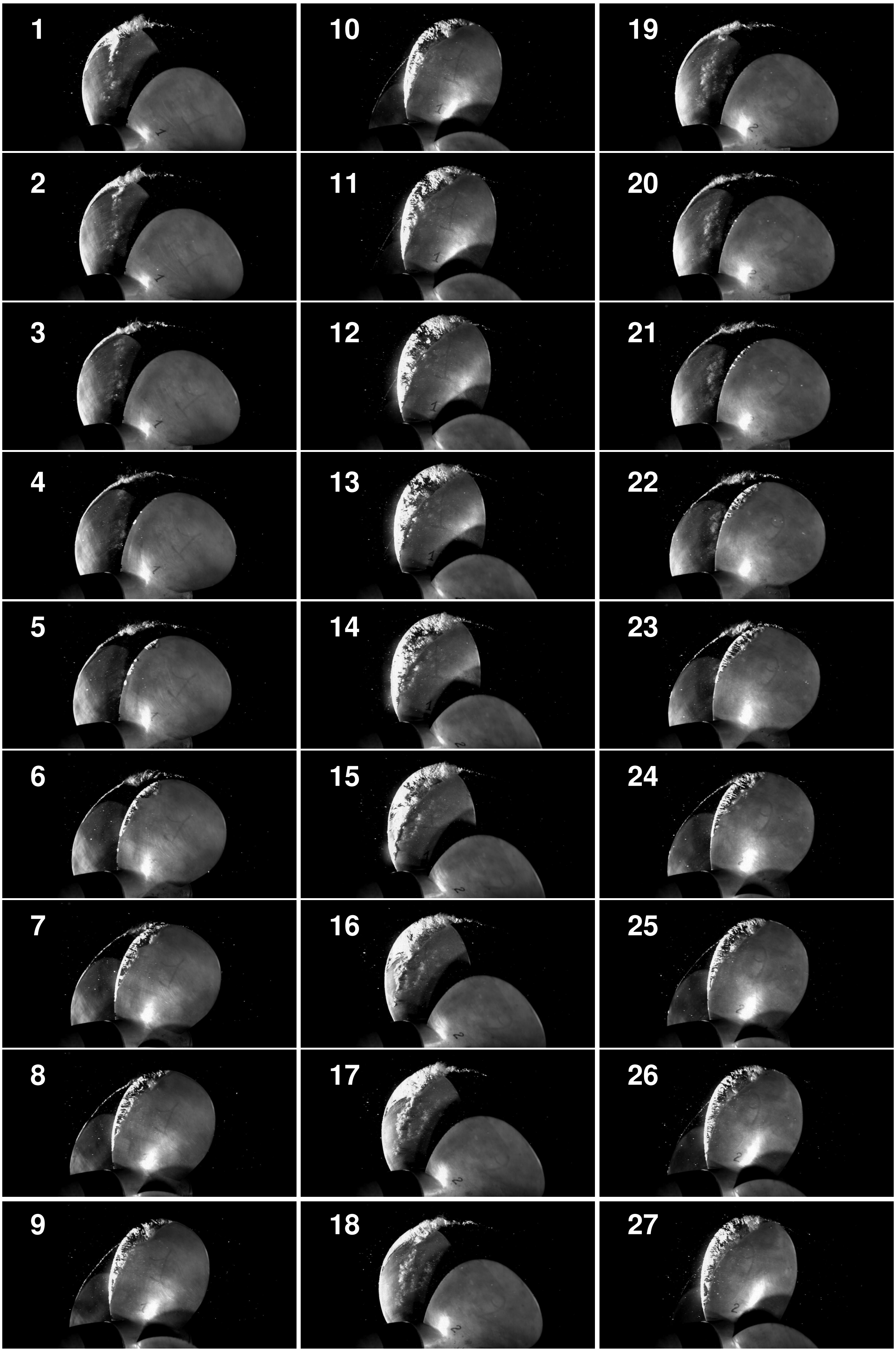

Figure 4. High-speed sequence of the cavitating propeller for $\sigma_0 = 3.5$. Interframe time= 500 µs, angular step= 5.4°. Flow is from left to right, and view is from propeller backface, portside. Wake generator is on the left.

Peer-reviewed version available at J. Mar. Sci. Eng. 2016, 4, 70; doi:10.3390/jmse4040070

in the longitudinal, vertical plane of symmetry at a distance of about one diameter downstream of the propeller plane. They are placed radially at 80 mm ≈ 0.7R (H_1), 100 mm ≈ R (H_2), 120 mm (H_3) and 200 mm (H_4) from the propeller axis, see Fig. 5. H_1 and $H3$ are respectively inside and outside the slipstream, while H_2 is roughly located at the tip vortex position, and H_4 is purposedly distant from the flow perturbation created by the propeller.

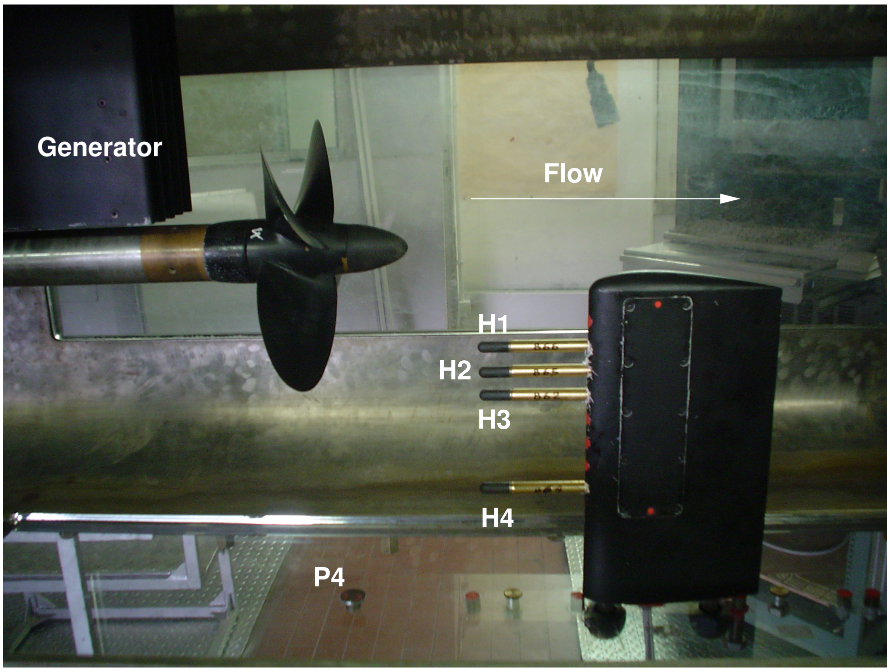

Figure 5. Hydrophone strut for inflow pressure measurement.

The wall pressure transducers are calibrated statically in pressure and tension. The discrepancy between the measured and the actual value is less than 0.5% across the full pressure range. A dynamic calibration has also been performed for the hydrophones to verify the manufacturer's calibration sheet. These hydrophones provide a measurement uncertainty of ±1.5 Pa re µPa in the range 10 Hz to 80 kHz and a frequency response flat in the range 0.1 Hz to 20 kHz with a tolerance of -1.5 to +1 dB re µPa.

The signals are sampled at a rate of 100 kHz per channel and recorded for 30 seconds, during which the propeller performs about 900 revolutions. As a consequence, we have a sample of all eight signals approximately every 0.11° of propeller rotation.

4.2. Harmonic Analysis of Pressure Data

Pressure signals are sampled N times per propeller revolution with a time step $\Delta t = 10^{-5}$ s, corresponding to the preset sampling frequency of the data acquisition system. A waveform is then constructed by ensemble averaging with the following relation:

$$\overline{\mathbf{P}}_{\theta_i} = \frac{1}{M}\sum_{m=1}^{M}\overline{P}_{\theta_i,m} \quad \text{with} \quad \theta_i \in [60^\circ, 120^\circ] \tag{1}$$

where $\overline{\mathbf{P}}_{\theta_i}$ is the ensemble-averaged pressure corresponding to angular phase θ_i. The summation is done over the M revolutions and $\overline{P}_{\theta_i,m}$ is the average pressure value for the m$^{\text{th}}$ revolution calculated over the angular slot centered at θ_i. M is approximately 900, whereas the angular slot width is in the interval $[\theta_i - 2.5^\circ, \theta_i + 2.5^\circ]$.

Since the process described by Eq. (1) is 2π-periodic, we can apply Fourier's harmonic analysis. Expressed in mathematical terms, a periodic function $g(t)$ of fundamental frequency f_0 can be written

Peer-reviewed version available at J. Mar. Sci. Eng. 2016, 4, 70; doi:10.3390/jmse4040070

as an infinite sum of sine or cosine functions in the interval $[-\pi, +\pi]$. Specifically, we can use the cosine function such that

$$g(t) = \sum_{n=0}^{\infty} A_n \cos(2\pi n f_0 t + \phi_n) \tag{2}$$

where A_n and ϕ_n are the amplitude and phase of the n^{th} harmonic function, respectively. Equation (2) can be rephrased as

$$g(t) = \sum_{n=0}^{\infty} C_n \cos 2\pi n f_0 t \quad + \quad \sum_{n=0}^{\infty} S_n \sin 2\pi n f_0 t \tag{3}$$

where A_n and ϕ_n are now replaced by the Fourier coefficients C_n and S_n, which are calculated using the following formulæ:

$$C_0 = f_0 \int_{-f_0/2}^{f_0/2} g(t) dt, \qquad \left. \begin{aligned} C_n &= 2 f_0 \int_{-f_0/2}^{f_0/2} g(t) \cos 2\pi n f_0 t \, dt \\ S_n &= 2 f_0 \int_{-f_0/2}^{f_0/2} g(t) \sin 2\pi n f_0 t \, dt \end{aligned} \right\} \quad \text{for} \quad n > 0 \tag{4}$$

This transform allows the decomposition of a signal into its periodic components, i.e. the fundamental frequency or first harmonic, and its multiples or higher order harmonics. Such an analysis of a periodically unsteady flow-field sorts out the phase-locked coherent flow features. The fundamental is in our case embodied by the blade passage frequency, hereafter called BPF, which is equal to the rotation frequency times the number of blades. The propeller is rotating at 30 Hz and the number of blades is four, therefore BPF is equal to 120 Hz. The actual rotation period is estimated based on the mean period registered between consecutive propeller trigger pulses, for the angular velocity is subject to a slight jitter due to the variable hydrodymanic loading.

5. Results and Discussion

5.1. Cavitation Pattern

Figure 6 represents the evolution of the mean cavity extension S_c as a function of the blade angular position θ. The cavity area is represented in terms of a non-dimensional value, where the actual area has been normalized by S_0 defined as the blade area for $r/R \geq 0.3$, r being the radial coordinate and R the propeller radius. We report the mean value of the cavity extension over the blade and its root-mean-squareCalculation and Comparison of Propeller Ubsteady Pressure Forces on Ships deviation. We recall that the cavity extension is calculated in angular slots of 5°, which matches closely the angular resolution of the high-speed visualizations, see Section 3. Also note that each value is the average over about 900 instantaneous acquisitions, one per propeller rotation. It is important to appreciate that this figure is unique in that it represents the first instance where a quantitative measure of the leading edge cavity is reported in literature in the case of a cavitating marine propeller.

It is seen that leading edge cavitation occurs before 60°, however inception and initial expansion are not captured as the optical access is limited to the interval [60°, 120°], see Section 3. The cavity grows as the blade approaches the vertical position where it enters the wake region, reaching a maximum located beyond the 12-o'clock position (up 90°). As the cavitation number is further decreased, this peak deviates in the direction of the propeller rotation, moving from about 90° for σ_0=7.5 to 105° for σ_0=2.5. Note the larger fluctuations in the region beyond 100°, as discussed below.

Figure 7 shows the evolution of the root-mean-square of the cavity area S_c. A main peak is observed after the vertical position, and is assignable to the collapse of the main cavity, with vapor clouds that detach from the leading edge and merge with the tip vortex, see Fig. 4 from frames 10 to

Peer-reviewed version available at J. Mar. Sci. Eng. 2016, 4, 70; doi:10.3390/jmse4040070

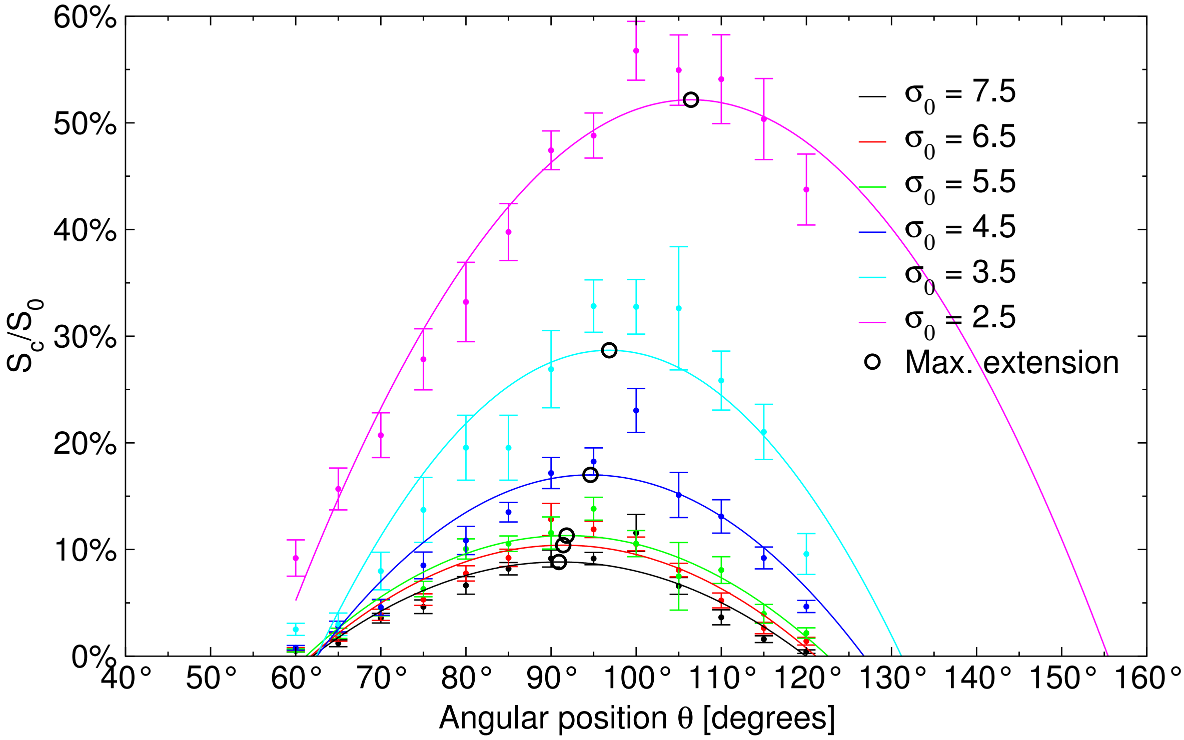

Figure 6. Cavity extension and corresponding root-mean-square fluctuations as a function of the propeller angle θ and for $\sigma_0 \in [2.5, 7.5]$. The continuous lines are quadratic fit curves to the respective experimental data. The black circles indicate the location of the cavity maximum extension calculated from the fit function.

20. Note that the cavity is mostly attached and within the blade surface. As the cavitation number is decrease below 4.5, a second peak appears around $\theta \approx 80^\circ$, and is linked to the narrow turbulent shear layer shed from the portside plate of the wake simulator. From that point onward, the cavity extends along the leading edge towards the blade tip where it merges with the tip vortex, thence expanding over the trailing edge into the fluid, as shown in the same sequence.

5.2. Pressure Field

Figure 8 shows the integral energy E_{Total} of the pressure signal as a function of the cavitation number σ_0, with $E_{Total} = \sum A_i^2$ for $i > 0$. The constant term A_0 being discarded, each point represents the energetic contribution of the fluctuating part of the signal, as per the Parseval's theorem applied to the Fourier series.

In terms of wall pressure (top plot), P_2 records the highest energy content due to its close vicinity to the cavitating blade tips. Also, all but P_3 tend to collapse to the same level at about 10^5 Pa^2 towards non-cavitating conditions, i.e. high σ_0. We observe a general increase of the energy with decreasing σ_0, which is consistent with an expanding cavitation pattern and more intense collapse events. A clear change in trend occurs between σ_0=4 and 5. This is related in part with the cavitation disturbance caused by the blade entry into the sharp shear layer on the wake simulator portside. It is also related with the occurrence of the so-called bursting cavitation [15], i.e. by the growth and collapse of a detached vapor structure in the interblade space, as seen in Fig. 4. For cavitation numbers where the bubble extends beyond the trailing edge and closes in the bulk of the fluid, the pressure energetic content tends to stagnate or even decrease. This transition is visible in Fig. 8 where we observe a plateau below $\sigma_0 = 2$ for the P-probes. This behavior is not seen on the energy plot of the pressure recorded in the wake (H transducers). In fact, within the slipstream, the kinetic pressure induced by the propeller is largely dominant. For this reason, H_1 and H_2 display higher energy levels than

Peer-reviewed version available at J. Mar. Sci. Eng. 2016, 4, 70; doi:10.3390/jmse4040070

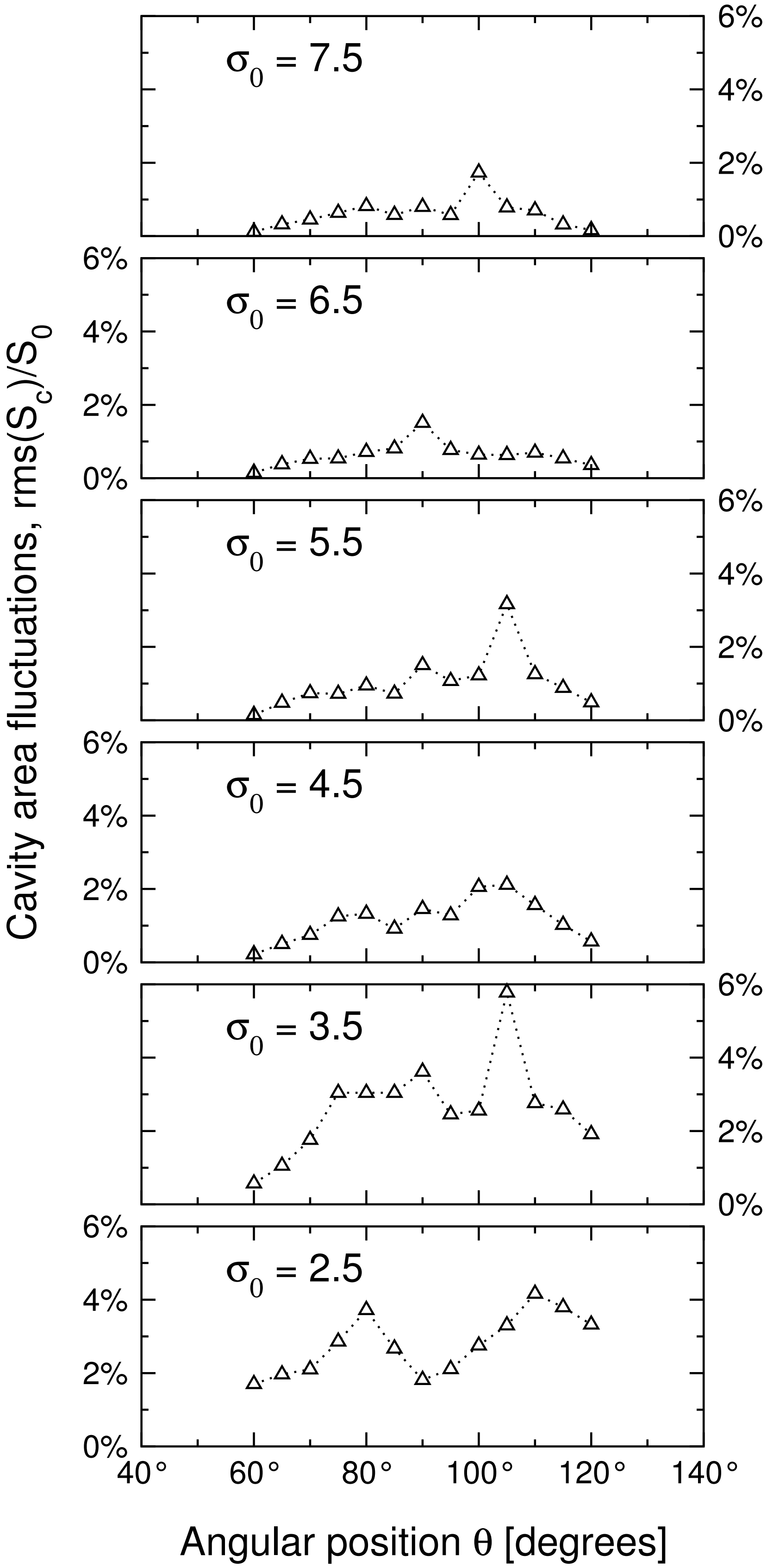

Figure 7. Fluctuations of the cavity extension as a function of the propeller angle θ.

Peer-reviewed version available at J. Mar. Sci. Eng. 2016, 4, 70; doi:10.3390/jmse4040070

H_3 and H_4, which are mostly sensitive to the overall noise scattered in the test section. H_1 senses essentially the turbulent shear wake originating from the blades' trailing edge [20]. H_2 is one order of magnitude more energetic than H_1, as it is located in the region swept by the blades' tip vortices.

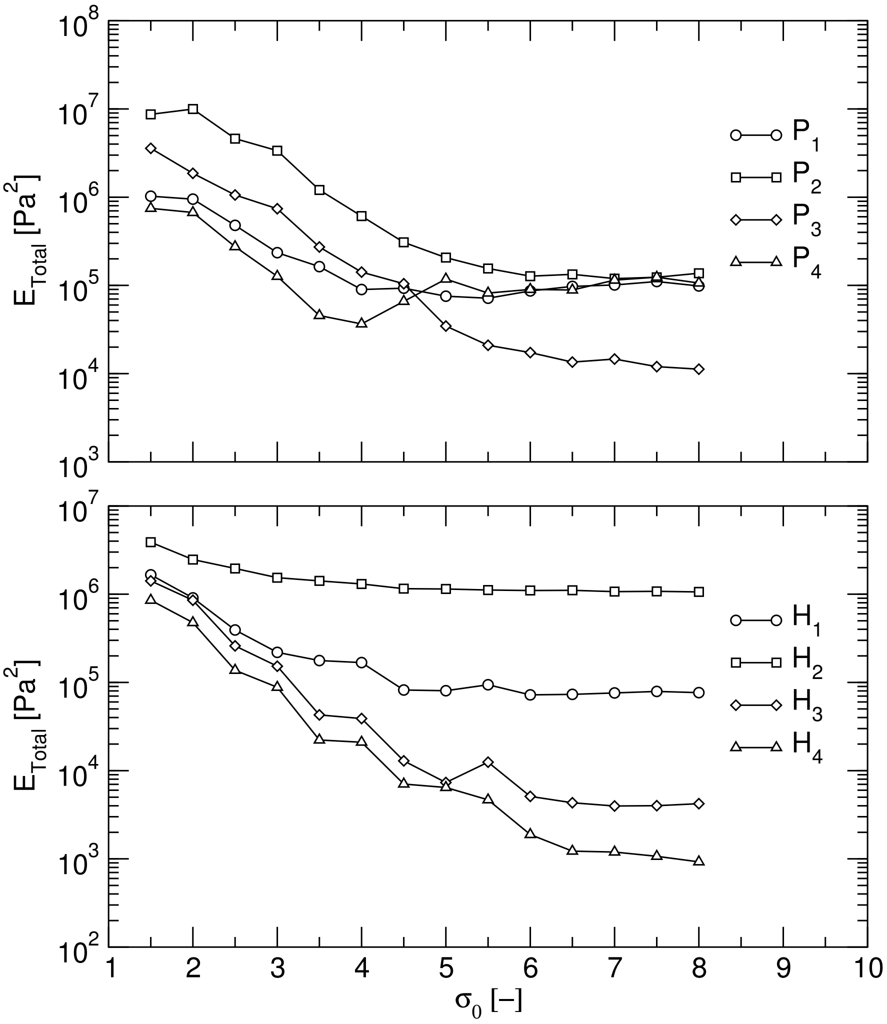

Figure 8. Energy integral of the fluctuating pressure versus the cavitation number at the wall (P probes, top) and in the fluid (H probes, bottom).

For the sake of conciseness, we will focus our harmonic decomposition on the H_2 and P_2 probes, as they display the most energetic content. Figures 9 and 10, respectively relative to H_2 and P_2, report the ensemble mean and fluctuating parts of the pressure in a polar form representating one propeller rotation. In these plots, 0° represents the phase start as indicated in Fig. 1, and 90° is the mean location of the flow perturbation created by the wake generator. The first and second order statistics are calculated using Eq. (1). Each polar plot is accompanied by a graph of the amplitude A_n, which is equal to the norm of the vector (C_n, S_n), as per Eqs. (2) and (4), with n being a multiple of the blade harmonic (BPF, blade passage frequency). Plots are presented for all values of the cavitation number σ_0, from reduced leading edge cavitation at σ_0=7.5 to extended cavitation at σ_0=1.5.

The two locations display very distinct behaviors. H_2 is naturally sensitive to the passage of the tip vortex generated by the blades, due to its location at about one propeller radius. For this reason, the first blade harmonic is clearly preponderant in all conditions. We note that the energy distribution amongst the different orders remains mostly unchanged for $\sigma_0 > 4.5$ and is increased by 50% as σ_0 reaches 1.5. The second harmonic remains mostly unchanged for a cavitation number larger than 2.0, where its contribution almost vanishes to reappear at $\sigma_0 = 1.5$ along with strong third and fourth

Peer-reviewed version available at J. Mar. Sci. Eng. 2016, 4, 70; doi:10.3390/jmse4040070

harmonics, corresponding to 12 and 16 times the rotation frequency. This pattern could be related to the occurrence of the bursting phenomenon that becomes dominant over the attached cavitation at low σ_0. Higher harmonics are also activated as the cavitation number σ_0 goes under 4.5, with some emphasis on harmonics beyond the fourth order as one would expect in presence of a cavitating tip vortex [6]. However, the energy partition is dominated by the first harmonics, that is by the flow dynamics governed by the blade passage frequency.

The graphs of the harmonic amplitude for the wall pressure location P_2 show a pressure pattern that is strongly correlated with the cavitation state, for the sensor is located closest to the propeller blade. Again, there is a clear change as σ_0 is brought below 4.5. Below this threshold, the energy is progressively increasing in harmonic orders, with a rich content up to the 12^{th} and beyond. This part of the energy spectrum becomes preponderant between 3.5 and 2.0, with a clear presence of the third and fourth harmonics as also observed in Fig. 9. This supports our observation that there exists a modulation of the BPF by the bursting structure released in the interblade space. High frequency content above the fourth harmonic, is linked to the tip vortex dynamics and to the implosion of bubble clouds rather than to the larger scale leading edge cavitation. As σ_0 approaches 1.5, the main cavity and the tip vortex merge into a single large vapor structure that behaves as a monopole scattering predominantly at the fundamental blade harmonic.

From the polar plots of P_2, it is observed that the pressure fluctuations (solid lines) present a periodic pattern that changes as σ_0 crosses the 4.5 threshold, see Fig. 10. In fact, the lobes progressively split to form a two-lobe pattern, see graphs at σ_0=4.5 and 4.0, with one peak gaining intensity as σ_0 is further decreased. This behavior is clearly related to the growth and collapse of the main cavity, as illustrated by the frames 10 to 19 of Fig. 4, followed by the growth and collapse of the bursting structure that occurs in the interblade space (frames 20 to 24). From these high-speed sequences, this bursting structure grows in intensity while the main cavity loses potential energy as it expands over and beyond the blade surface. The sequence of events described by the pressure patterns on P_2 suggests that the pressure pulses from the second series of collapses are stronger than those from the growth and implosion of the main cavity. Indeed, the high-speed sequence shows a smooth wipe-out of the attached cavity rather than a violent collapse, see frames 16 to 18 of Fig. 4. Instead the vapor structure that is shed away into the interblade fluid by this process interacts strongly with the tip vortex, feeding it with vapor matter that contributes to a violent secondary collapse in the fluid. This event takes place when the approaching blade is at about 60°, as shown in Fig. 10 by the sharp peak (solid line) visible on the polar graph at $\sigma_0 = 2.5$, and is the result of the collapse event originating from the preceding blade. This collapse occurs with varying delay, thus explaining the progressive phase change observed on the polar plots from $\sigma_0 = 3.0$ to $\sigma_0 = 2.0$. This phase-shift is not visible on the fluctuating pressure pattern of H_2, since the flow dynamics of the wake tube dominate over the cavitation events on the blade.

This phase-shift $\Delta\phi$ is particularly evident on the first harmonic of the signals, both on the mean and on the fluctuating parts. In Fig. 11, we report this quantity for the case of the mean term and with respect to off-cavitation conditions ($\sigma_0 = 8.0$). No significant change is observed for the pressure location H_2, as expected. However, P_2 exhibits a phase-shift clearly influenced by the cavity dynamics, as it increases with increasing cavity size, and points to delayed collapse events. The monotonous increase agrees with the fact that the growth-and-collapse cycle of the attached cavity develops over a longer period of time as σ_0 is decreased, see Fig. 6. However, this trend breaks at σ_0=3.0, which is consistent with our analysis that the series of collapses originating from the bursting vortex structures become predominant over those associated with the attached cavity.

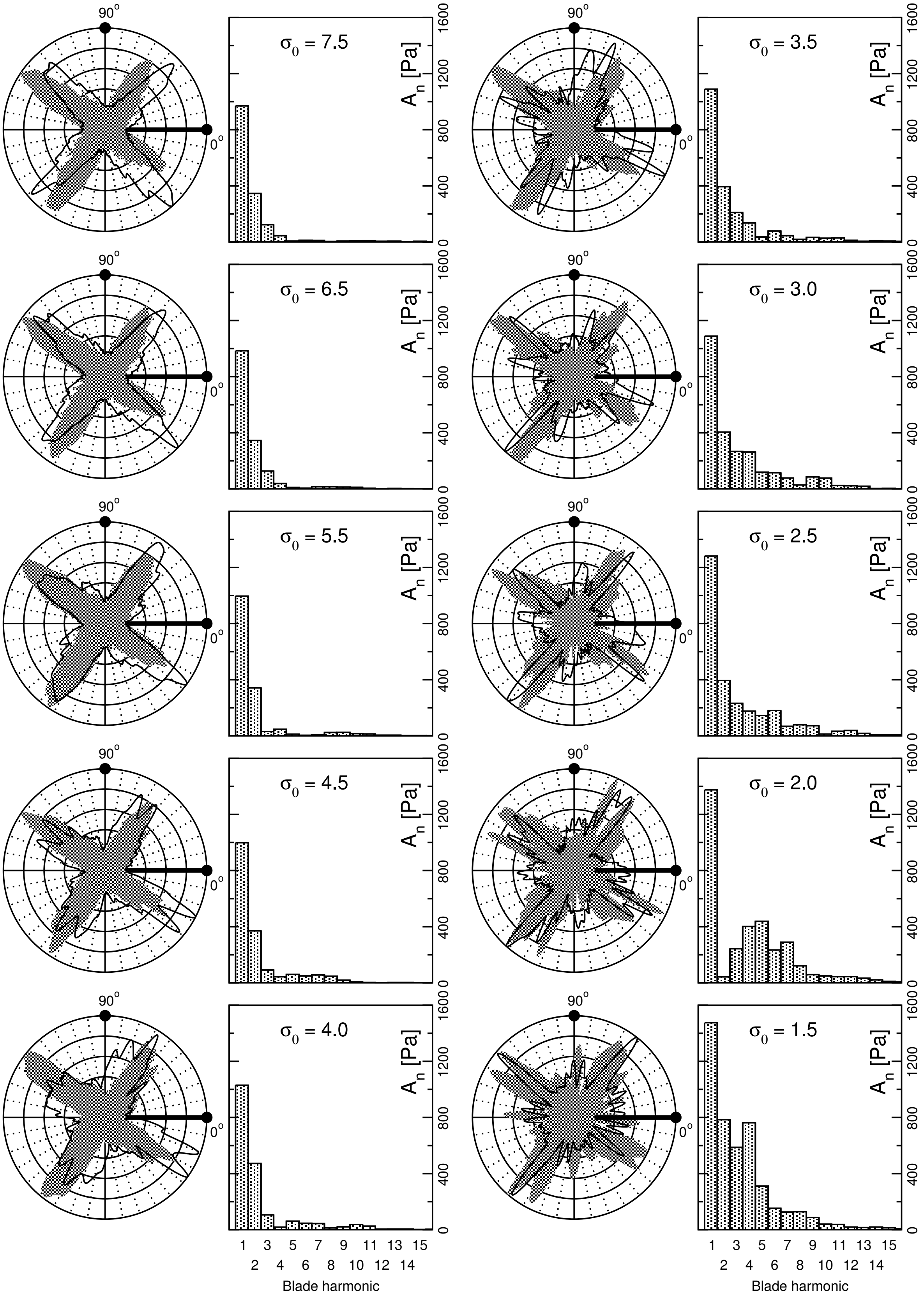

Figure 9. Angular history of the presssure signal from hydrophone H_2 and corresponding harmonic content, for different values of the cavitation number σ_0. The polar graphs are non-dimensionalized. Grey area: ensemble mean; solid line: ensemble fluctuations.

Peer-reviewed version available at J. Mar. Sci. Eng. 2016, 4, 70; doi:10.3390/jmse4040070

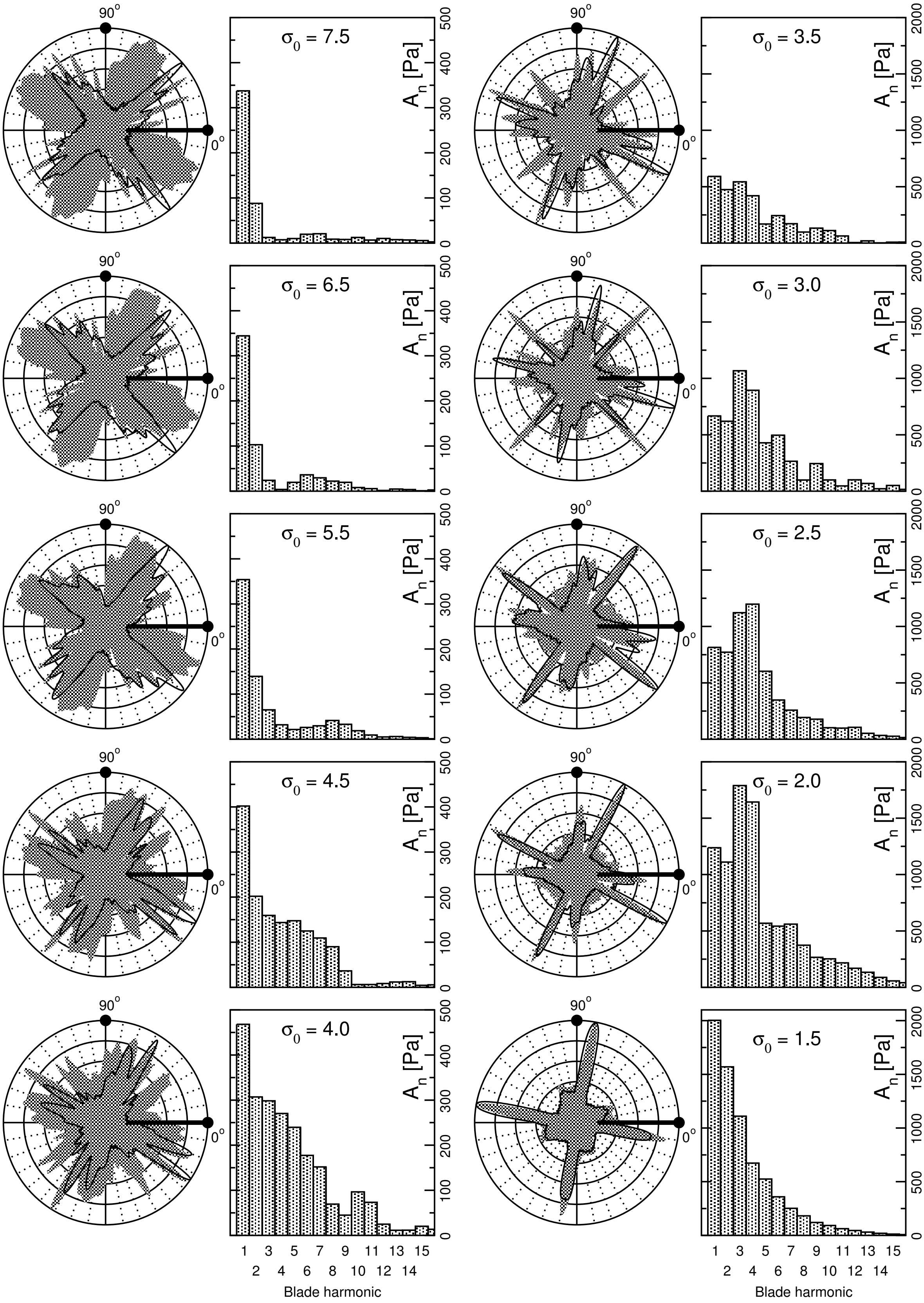

Figure 10. Angular history of the pressure signal from transducer P_2 and corresponding harmonic content, for different values of the cavitation number σ_0. The polar graphs are non-dimensionalized. Grey area: ensemble mean; solid line: ensemble fluctuations.

Peer-reviewed version available at J. Mar. Sci. Eng. 2016, 4, 70; doi:10.3390/jmse4040070

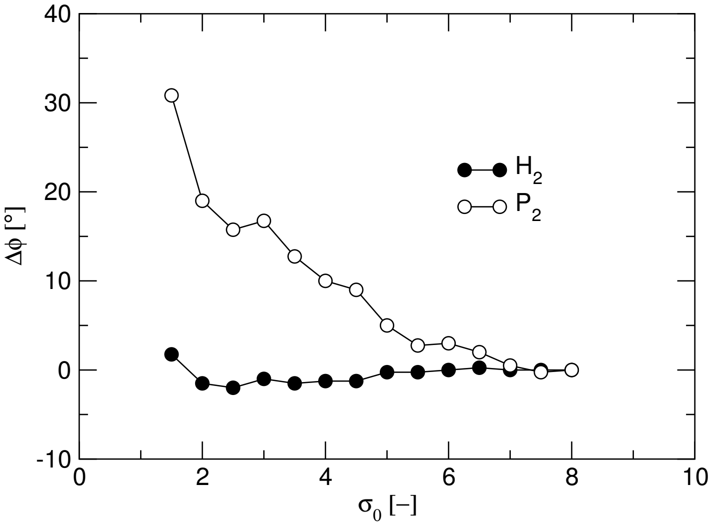

Figure 11. Phase-shift observed on the first harmonic component of the mean pressure, relative to the non-cavitating condition.

6. Correlations Between Cavitation and Pressure Field

6.1. Time Correlations

Previous works by Pereira *et al.* [22] showed that on bidimensional hydrofoils, the height of the leading edge cavity is linearly linked to its length. These authors also showed experimentally that the vapor structures generated by an unsteady sheet cavitation could also be embodied by a similar characteristic length. Further experimental observations and numerical simulations of cavitating propeller flows performed by Pereira *et al.* [23] brought also new evidence that the cavity thickness on a propeller blade had a similar behavior. We therefore make the hypothesis that the cavity volume V_c is proportional to a characteristic length l_c such that

$$V_c \propto l_c^3 \quad \text{with} \quad l_c = \sqrt{S_c} \tag{5}$$

where S_c is the cavity extension. Assuming that the cavity can be represented by an equivalent spherical bubble, we calculate the Rayleigh time T_c to collapse following:

$$T_c \propto l_c \sqrt{\frac{\rho}{P_\infty - P_v}} = \frac{l_c}{U_\infty}\sqrt{\frac{2}{\sigma_0}} \tag{6}$$

where l_c is taken as the bubble maximum radius at time 0, ρ is the fluid density and $P_\infty - P_v$ is the pressure gradient experienced by the bubble, which is recovered from σ_0 and the flow upstream velocity according to:

$$P_\infty - P_v = \frac{1}{2}\rho {U_\infty}^2 \sigma_0 \tag{7}$$

Figure 12 displays the joint angular history of the cavity extension and of the mean pressure measured at location P_2, as per Fig. 6 and Fig. 10 respectively. From these plots, we recover the phase difference between the angular position θ_c of the cavity maximum extension, given by the fit functions of Fig. 6 (black circles), and the phase angle θ_p of the main pressure lobe following that peak position. The corresponding time T_p is then simply derived from the propeller rotation speed n as

$$T_p = \frac{\theta_p - \theta_c}{2\pi \cdot n} \tag{8}$$

Peer-reviewed version available at J. Mar. Sci. Eng. 2016, 4, 70; doi:10.3390/jmse4040070

Let us introduce the non-dimensional times τ_c and τ_p, which we define as

$$\begin{aligned}\tau_c &= \frac{T_c - T_{c|\sigma_0=7.5}}{T_{c|\sigma_0=4.5} - T_{c|\sigma_0=7.5}}\\ \tau_p &= \frac{T_p - T_{p|\sigma_0=7.5}}{T_{p|\sigma_0=4.5} - T_{p|\sigma_0=7.5}}\end{aligned} \tag{9}$$

Figure 13 represents these two normalized times, showing that there is indeed a clear linear correlation between these quantities for $\sigma_0 \geq 4.5$, thus unequivocably demonstrating that the pressure peaks are the result of the leading edge cavity collapse. This unique result relates pressure fluctuations to the cavitation growth and collapse dynamics. It also shows that the spherical bubble model is a good descriptor of propeller cavitation, specifically in presence of leading edge cavitation.

For $\sigma_0 < 4.5$, interblade bursting vapor structures combined with extended blade cavitation enter into play to create a composite cavitation pattern. This is mirrored on the pressure angular distribution, see Fig. 12, by the occurrence of sharp pressure peaks distinct from the broad lobes characteristic of the blade cavitation, both on the mean and fluctuating (RMS) parts. These pressure peaks match with secondary cavity extension peaks already outlined from Fig. 7, and are the source of the broadband excitation at high blade harmonics, see Figs. 9 and 10.

However, and despite the fact that the collapse time is altered by different but coupled collapse events, a linear relatonship still seems to hold for this σ_0 range, see Fig. 13. This important observation indicates that such a complex pattern preserves, in its globality, the general characteristics of the bubble model. This opens the possibility to describe the complete cavitation behavior of a propeller, and consequently the complete near-field pressure peaks induced by cavitation, on the sole basis of this model.

6.2. Pressure from Vapor Volume

We propose here a model to predict the pressure fluctuations induced by cavitation, upon the concept of the pressure increment generated by an expanding spherical cavity, see e.g. Breslin *et al.* [10]. Assuming a spherically symmetric, irrotational, incompressible, radial flow emanating from a single point in a boundless fluid, the incremental pressure Δp at a given distance from an expanding cavity is shown, from first principles, to be proportional to the acceleration of the cavity volume V_c:

$$\Delta p \propto \frac{\partial^2 V_c}{\partial t^2} \tag{10}$$

Thus and following the definition of V_c given by Eq. (5), the volume acceleration can be written simply as

$$\frac{\partial^2 V_c}{\partial t^2} = 6\, l_c \left(\frac{\partial l_c}{\partial t}\right)^2 + 3\, l_c^2 \frac{\partial^2 l_c}{\partial t^2} \tag{11}$$

To verify the validity of this model, we choose the pressure data from location P_2, for it is closest to the blade occurrence and the richest in terms of energy content. In order to filter out effects not directly related to the attached cavitation, the pressure time signal from P_2 is reconstructed using only the first twelve harmonics. This choice is motivated by Figure 10 where most of the energy is concentrated in this range. The experimental cavity extension data is transposed to volume data following Eq. (5), thus fitted by a polynomial and derived twice numerically. This operation allows us to calculate the volume acceleration due to the cavity volume growth, as per Eq. (11). The estimated pressure increment Δp follows from Eq. (10) and is finally overlaid with the experimental Δp to produce the graphs shown in Fig. 14.

A striking agreement is found between the experimental and the computed values, in most of the time window covered by the cavity extension measurements. The estimated pressure variation derived from the cavity volume acceleration accurately matches the pattern of the measured Δp.

Peer-reviewed version available at *J. Mar. Sci. Eng.* **2016**, *4*, 70; doi:10.3390/jmse4040070

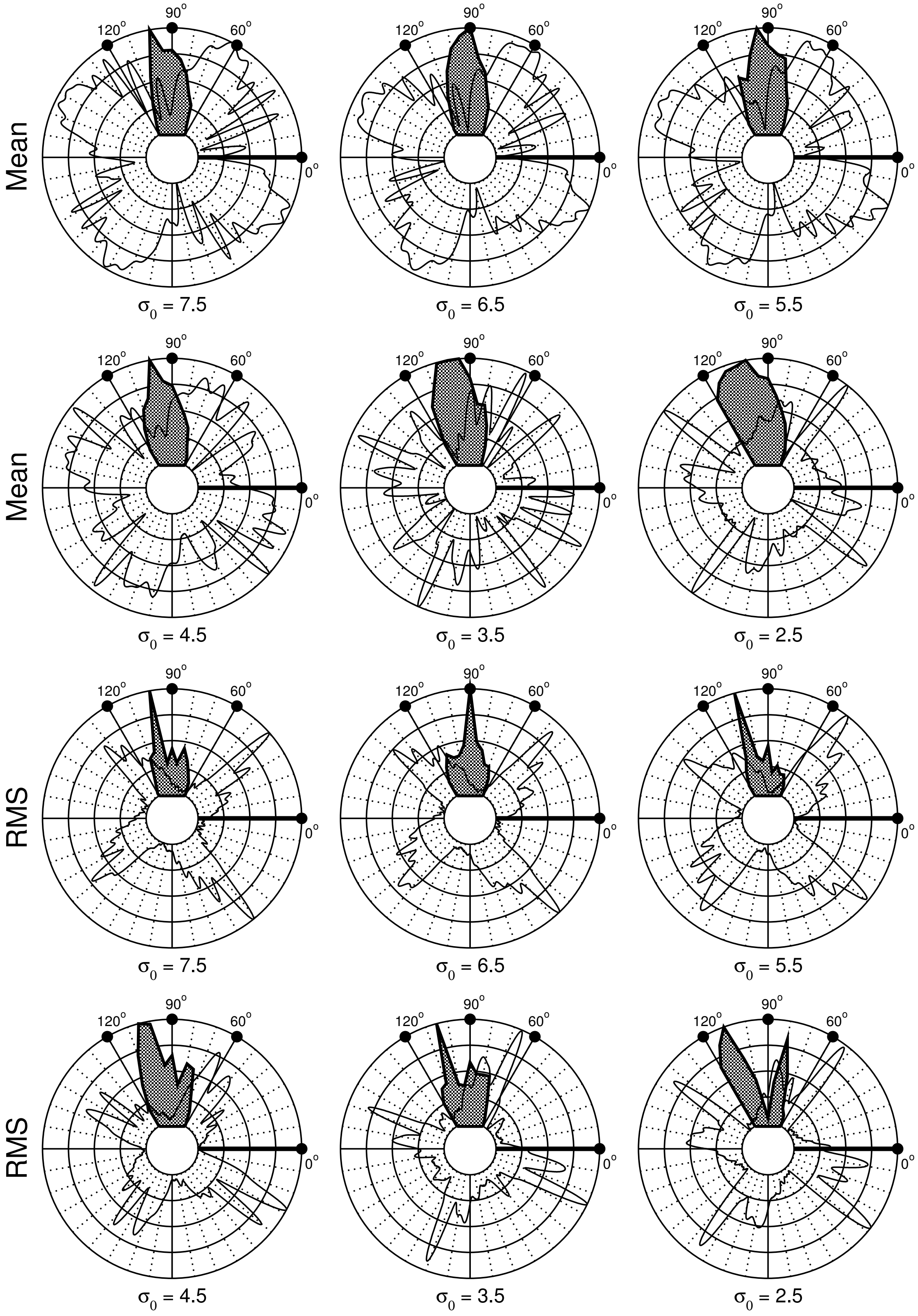

Figure 12. Pressure (P_2) and cavity extension correlations: mean (top two rows); fluctuations (bottom two rows). Cavitation area is represented by the grayed curve.

Peer-reviewed version available at J. Mar. Sci. Eng. 2016, 4, 70; doi:10.3390/jmse4040070

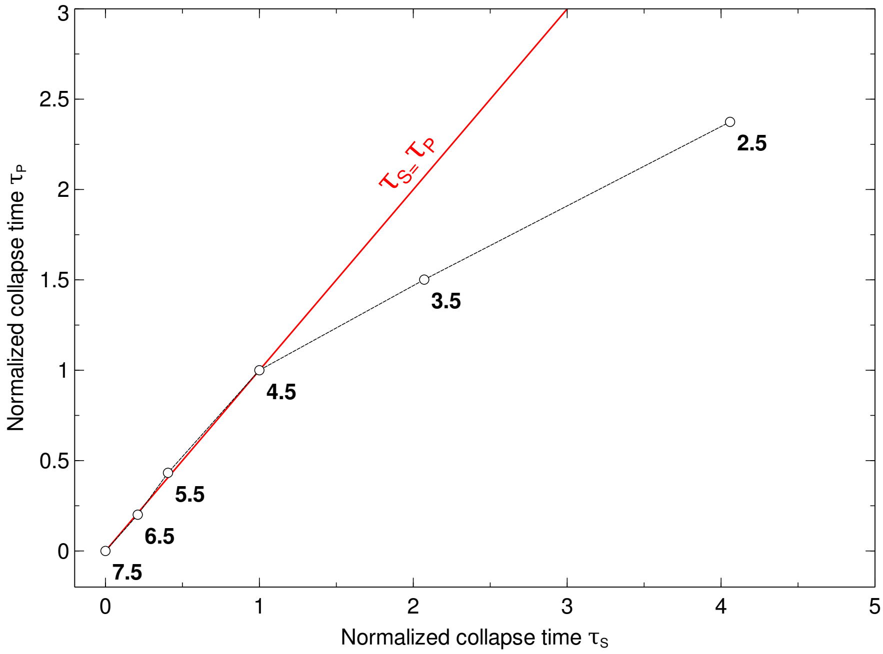

Figure 13. Comparison between the non-dimensional collapse times τ_c and τ_p, respectively calculated from the Rayleigh time as per Eq. (6), and from the time difference between cavity maximum extension and pressure peak. Labels report the value of the cavitation number σ_0. The red curve is the linear regression for $\sigma_0 \geq 4.5$.

Discrepancies are partly attributed to the chosen set of orders (12) used to reconstruct the pressure signal, and a more selective set of harmonics may improve the match. Most importantly, the detached vapor structures are not accounted for in the area measurement, therefore the reconstructed volume data and consequently the resulting derived pressure field can only be partial in terms of harmonic content. For instance, the bursting vapor structure that develops in the interblade space is not considered in this process. Yet, the pressure peaks and troughs are very well reproduced, especially in terms of phase and period. A very good match is also seen on the peak-to-peak values. Hence, the simple model of Eq. (10) is found to perform surprisingly well. This result further supports the idea that the measurement of the cavitation extension, despite being relatively simple and despite the complexity of the cavitation context, can provide the necessary information for the prediction of the pressure pulses in real cases.

Peer-reviewed version available at J. Mar. Sci. Eng. 2016, 4, 70; doi:10.3390/jmse4040070

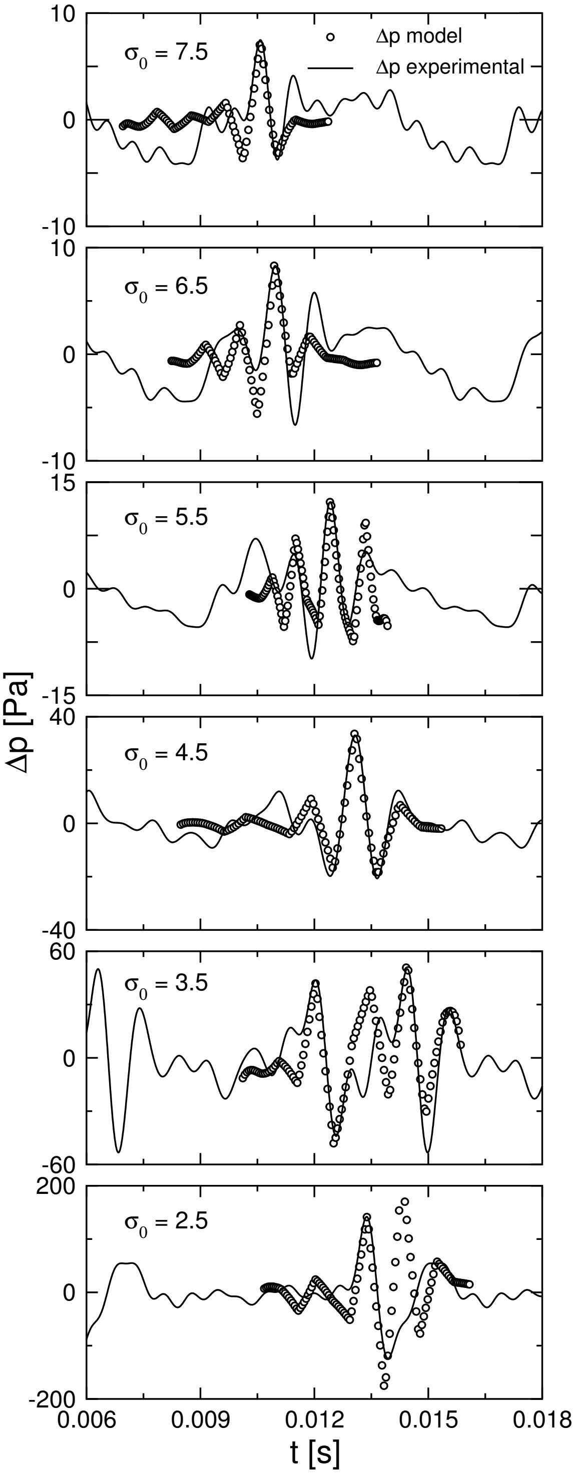

Figure 14. Comparison between measured Δp (___) and Δp estimated (○) from volume acceleration as per Eq. (11).

7. Conclusions

An experimental study of a cavitating propeller operating in a non-uniform flowfield has been presented. A wake simulator was used to create a local flow perturbation upstream of the propeller. Using four hydrophones placed downstream in the propeller wake and four wall-mounted pressure transducers in the propeller plane, a detailed harmonic analysis based on energetical considerations has put into evidence the contributions of flow features such as the leading edge cavity, the blade tip vortex, the blade wake and the bursting cavitation. Phase shifts linked to the cavitation dynamics, not yet documented to date, have been found and quantified. Though, this approach is clearly limited in its ability to separate and identify unambiguously the pressure sources. In this respect, the help of quantified time-resolved high-speed image recordings of the cavitation brings essential support. The mean and fluctuations of the leading edge cavitation extension have been established and have brought further support to the results of the harmonic analysis.

Upon the pressure and the cavitation extension data, we have established unambiguous time correlations between the pressure peak fluctuations and the cavity dynamics, by establishing a clear correspondence between the collapse time derived from the cavity volume and the time occurrence of the pressure peaks. Further, a model linking the cavity volume acceleration to the radiated pressure gradient was implemented. With the hypothesis of a characteristic length based upon the cavity extension, we were able to derive the cavity volumetric acceleration and compare the associated pressure increment with the actual pressure variation. A remarkable correspondence was found, suggesting that this model is a potentially very useful tool to estimate the propeller-induced pressure fluctuations from relatively simple observations of the blade cavitation pattern.

Acknowledgments: The authors are grateful to the personnel of the Italian Navy hydrodynamic facility (CEIMM, Rome). Acknowledgments also go to the undergraduate students who helped in the performance of this work: Mr Torquati from "Roma Tre" University (Rome, Italy); Mrs Bidault and Mrs Daloubeix from École Navale (Brest, France), under the supervision of Prof. J.-Y. Billard. The research has been partly financed through the Sixth EC framework program VIRTUE, Grant No. TIP5-CT-2005-516201. The work is presented as part of the CNR-INSEAN Propulsion Systems Work Package (CNR identification number ET.P02.018.002)

Appendix. Nomenclature

Symbol	Description	Units
U_∞	Upstream axial inflow velocity	$\mathrm{m\,s^{-1}}$
D	Propeller diameter, $2R$	m
R	Propeller radius	m
n	Propeller rotation frequency	Hz
p_0	Pressure at propeller axis	Pa
p_v	Vapor pressure	Pa
J	Advance coefficient, U_∞/nD	-
ρ	Fluid density	$\mathrm{kg\,m^{-3}}$
σ_0	Cavitation number referred to U_∞, $(p_0 - p_v)/0.5\rho U_\infty^2$	-
S_c	Cavity extension	$\mathrm{m^{-2}}$
l_c	Cavity characteristic length	m
V_c	Cavity volume	$\mathrm{m^{-3}}$
T	Thrust	N
S_0	Blade area for $r/R \geq 0.3$	$\mathrm{m^{-2}}$
K_T	Thrust coefficient, $T/\rho n^2 D^4$	-
A_n, ϕ_n	Amplitude and phase of the Fourier series	Pa, °
C_n, S_n	Coefficients of the Fourier series	Pa
f_0	Fundamental frequency	Hz
BPF	Blade passage frequency	Hz
θ	Angular position	°

Bibliography

1. Pereira, F.; Salvatore, F.; Di Felice, F. Measurement and Modelling of Propeller Cavitation in Uniform Inflow. *J. Fluids Eng.* **2004**, *126*, 671–679.

2. Ito, T. An Experimental Investigation into the Unsteady Cavitation of Marine Propellers. *Report of the Ship Research Institute* **1966**, *11*, 1–18.
3. Takahashi, H.; Ueda, T. An Experimental Investigation into the Effect of Cavitation on Fluctuating Pressure around a Marine Propeller. Proc. Twelfth International Towing Tank Conference; ITTC, National Academy Press, Washington, D.C., USA: Rome (Italy), 1969; pp. 315–317.
4. Huse, E. Pressure Fluctuations on the Hull Induced by Cavitating Propellers. Technical Report 111, Norwegian Ship Model Experiment Tank, 1972.
5. Dyne, G. Study of the Scale Effect On Wake, Propeller Cavitation, and Vibratory Pressure at Hull of Two Tank. *SNAME Transactions* **1974**.
6. Bark, G.; Berlekom, W.B. Experimental Investigations of Cavitation Dynamics and Cavitation Noise. Proc. Twelfth Symposium on Naval Hydrodynamics; ONR, Statens skeppsprovningsanstalt: Göteborg (Sweden), 1978; Meddelande från Statens skeppsprovningsanstalt, pp. 470–493.
7. Matusiak, J. Broadband Noise of the Cavitating Marine Propellers: Generation and Collapse of the Free Bubbles Downstream of the Fixed Cavitation. Proc. Nineteenth Symposium on Naval Hydrodynamics; Sponsored by Office of Naval Research, USA; National Research Council, USA; and Soc Naval Architects of Korea, National Academy Press, Washington, D.C., USA: Seoul (Korea), 1992; pp. 701–712.
8. Johnsson, C.A.; Rutgersson, O.; Olsson, S.; Björheden, O. Vibration Excitation Forces From a Cavitating Propeller. Model and Full Scale Tests on a High Speed Container Ship. Proc. Eleventh Symposium on Naval Hydrodynamics; Office of Naval Research, National Academy Press, Washington, D.C., USA: London (UK), 1976; Vol. VIII, pp. 43–74.
9. Chiba, N.; Sasajima, T.; Hoshino, T. Prediction of Propeller-Induced Fluctuating Pressures and Correlation with Full Scale Data. Proc. Thirteenth Symposium on Naval Hydrodynamics; Office of Naval Research, National Academies Press, Washington, D.C., USA and The Shipbuilding Research Association of Japan, 1981: Tokyo (Japan), 1980; pp. 89–103.
10. Breslin, J.P.; Van Houten, R.J.; Kerwin, J.E.; Johnsson, C.A. Theoretical and Experimental Propeller-Induced Hull Pressures Arising from Intermittent Blade Cavitation, Loading, and Thickness. *SNAME Transactions* **1982**, *90*, 111–151.
11. Kurobe, Y.; Ukon, Y.; Koyama, K.; Makino, M. Measurement of Cavity Volume and Pressure Fluctuation on a Model of the Training Ship ”SEIUN MARU” with Reference to Full Scale Measurement. *Report of the Ship Research Institute* **1983**, *20*, 395–429.
12. Friesch, J.; Johannsen, C.; Payer, H.G. Correlation Studies on Propeller Cavitation Making Use of a Large Cavitation Tunnel. *SNAME Transactions* **1992**, *100*, 65–92.
13. Friesch, J. Correlation Investigations for Higher Order Pressure Fluctuations and Noise for Ship Propellers. Proc. Third International Symposium on Cavitation; Michel, J.M.; Kato, H., Eds.; Université Joseph Fourier, Grenoble, France: Grenoble (France), 1998; pp. 259–265.
14. Johannsen, C. Investigation of Propeller-Induced Pressure Pulses by Means of High-Speed Video Recording in the Three-Dimensional Wake of a Complete Ship Model. Proc. Twenty-Second Symposium on Naval Hydrodynamics; Office of Naval Research, National Academy Press, Washington, D.C., USA: Washington, D.C. (USA), 1998; pp. 314–329.
15. Konno, A.; Wakabayashi, K.; Yamaguchi, H.; Maeda, M.; Ishii, N.; Soejima, S.; Kimura, K. On the mechanism of the bursting phenomena of propeller tip vortex cavitation. *Journal of Marine Science and Technology* **2002**, *6*, 181–192.
16. Paik, B.G.; Kim, K.Y.; Lee, J.Y.; Lee, S.J. Analysis of unstable vortical structure in a propeller wake affected by a simulated hull wake. *Experiments in Fluids* **2010**, *48*, 1121–1133.
17. Berger, S.; Bauer, M.; Druckenbrod, M.; Abdel-Maksoud, M. Investigation of Scale Effects on Propeller-Induced Pressure Fluctuations by a Viscous/Inviscid Coupling Approach. Proc. Third International Symposium on Marine Propulsors; Binns, J.; Brown, R.; Bose, N., Eds.; Australian Maritime College, University of Tasmania: Launceston, Tasmania (Australia), 2013; pp. 209–217.
18. Ji, B.; Luo, X.; Peng, X.; Wu, Y.; Xu, H. Numerical analysis of cavitation evolution and excited pressure fluctuation around a propeller in non-uniform wake. *International Journal of Multiphase Flow* **2012**, *43*, 13–21.

19. Ji, B.; Luo, X.; Wu, Y. Unsteady cavitation characteristics and alleviation of pressure fluctuations around marine propellers with different skew angles. *Journal of Mechanical Science and Technology* **2014**, *28*, 1339–1348.
20. Cotroni, A.; Di Felice, F.; Romano, G.P.; Elefante, M. Investigation of the Near Wake of a Propeller Using Particle Image Velocimetry. *Exp. Fluids* **2000**, *29*, S227–S236. Suppl.
21. Huse, E., Ed. *Report of the Twenty-First ITTC Cavitation Committee*, Vol. 1, Trondheim (Norway), 1996. National Academy Press, Washington, D.C., USA.
22. Pereira, F.; Avellan, F.; Dupont, P. Prediction of Cavitation Erosion: An Energy Approach. *J. Fluids Eng.* **1998**, *120*, 719–727.
23. Pereira, F.; Salvatore, F.; Di Felice, F.; Elefante, M. Experimental and Numerical Investigation of the Cavitation Pattern on a Marine Propeller. Proc. Twenty-Fourth Symposium on Naval Hydrodynamics; Office of Naval Research and West Japan Society of Naval Architects, National Academies Press, Washington, D.C., USA: Fukuoka (Japan), 2002; Vol. 3, pp. 236–251.